

**Supporting Information:**  
**Insights into pressure tunable reaction rates for electrochemical reduction of  
CO<sub>2</sub> in organic electrolytes**

Charles I. Shaughnessy<sup>a,b</sup>, David J. Sconyers<sup>a,c</sup>, Hyun-Jin Lee<sup>a</sup>, Bala Subramaniam<sup>a,b\*</sup>,  
James D. Blakemore<sup>a,c\*</sup>, and Kevin C. Leonard<sup>a,b\*</sup>

<sup>a</sup>Center for Environmentally Beneficial Catalysis, The University of Kansas, Lawrence, KS,  
USA

<sup>b</sup>Department of Chemical & Petroleum Engineering, The University of Kansas, Lawrence,  
KS, USA

<sup>c</sup>Department of Chemistry, The University of Kansas, Lawrence, KS, US

E-mail: bsubramaniam@ku.edu, blakemore@ku.edu, kcleonard@ku.edu

## 1 Detailed Discussion on Electrochemical Impedance Spectroscopy Data

Electrochemical Impedance Spectroscopy (EIS) was performed to quantify the pressure-dependent ohmic resistance of the Au/CXE system (Figs. S3 to S5). The ohmic resistance was taken as the offset of the real part of the impedance, as shown in the insets of Figures S3 to S5. In addition, the EIS data were modeled using a Randles equivalent circuit model, as shown in Fig. S2. The experimental data were fit to the Randles equivalent circuit using PyEIS.<sup>1</sup> The optimized parameters for the Randles circuit at each pressure and bias voltage are shown in Tables S1 to S3.

The Randles equivalent circuit contains a resistor representing the ohmic (or series) resistance ( $R_s$ ), a constant phase element (CPE), a resistance for charge transfer ( $R_{ct}$ ), and a Warburg element ( $Z_W$ ). The impedance for the constant phase element and Warburg element are shown in Equation (1) and Equation (2), respectively:<sup>1</sup>

$$Z_{CPE} = \frac{1}{Q_0(j\omega)^n} \quad (1)$$

$$Z_W = \sigma\omega^{-1/2} - j\sigma\omega^{-1/2} \quad (2)$$

where  $Q_0$  is the CPE constant,  $\omega$  is the frequency,  $j$  is the imaginary unit, and  $\sigma$  is the Warburg coefficient.

The key finding from the equivalent circuit modeling is that the ohmic resistance increases gradually between ambient conditions (ca. 2800  $\Omega$ ) and the optimum CO<sub>2</sub> pressure of 3.1 MPa (ca. 4100  $\Omega$ ). However, beyond this 3.1 MPa, the ohmic resistance increases more sharply to ca. 13000  $\Omega$  at 5.1 MPa. In addition, at each pressure, the ohmic resistance is not dependent on potential, providing additional evidence that the ohmic resistance of the system is caused by increasing the CO<sub>2</sub> pressure, and that beyond 3.1 MPa, the ohmic resistance is a significant contributor to attenuation of the CO<sub>2</sub> reduction rate. Moreover, the equivalent circuit model provides insights into the charge-transfer resistance ( $R_{ct}$ ), which is related to the kinetics associated with charge transfer. At all three pressures, the charge-transfer resistance decreases as the potential becomes

more negative, which is intuitive because the Butler-Volmer kinetic rate constant increases with more negative potentials for reduction reactions. The values of  $R_{ct}$  near the onset potential for  $\text{CO}_2$  reduction (ca.  $-2.2$  V vs  $\text{Fc}^+/\text{Fc}$ ) are similar at ambient pressure ( $2.2 \times 10^5 \Omega$ ) and at 3.1 MPa ( $2.6 \times 10^5 \Omega$ ). However, at 5.1 MPa the charge-transfer resistance  $-2.2$  V vs  $\text{Fc}^+/\text{Fc}$  increases by approximately one order of magnitude to  $3.2 \times 10^6 \Omega$ . This agrees very well with our finding from the COMSOL-based mechanistic model that the kinetic rate constant for the first reduction step remains essentially the same from atmospheric  $\text{CO}_2$  pressure to 3.1 MPa, but decreases by an order of magnitude at 5.1 MPa. Lastly, the Warburg impedance is usually a measure of mass-transfer limitations in of the system and is typically indicated by a  $45^\circ$  line in the EIS Nyquist plot. However, as shown in the simulations in Fig. S6, if the process is kinetically limited, only an upper-bound can be provided for the Warburg coefficient. None of the EIS data show the typical Warburg mass-transfer limitations, which is to be expected for  $\text{CO}_2$  reduction on a non-porous, polycrystalline Au electrode. Hence, only estimations of the upper limit of the Warburg coefficient were determined.

## 2 Supporting Tables and Figures

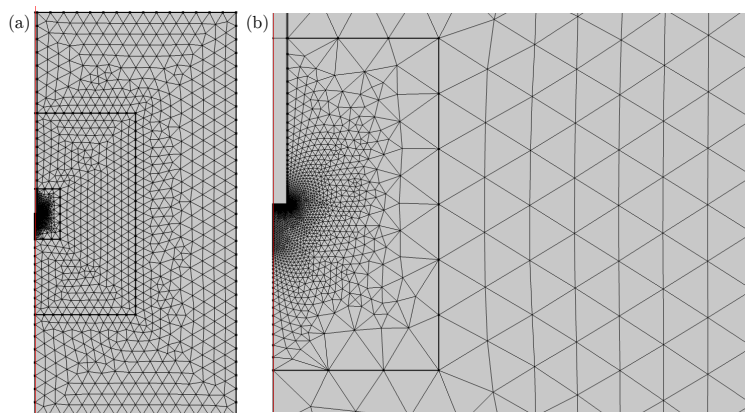


**Figure S1.** COMSOL reactor geometry and mesh showing the full simulation space (a) and a zoomed image around the simulated electrode (b).

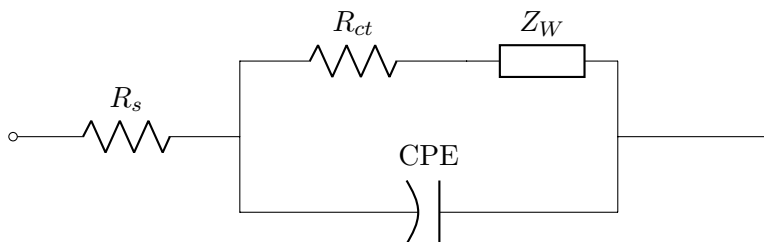


**Figure S2.** Randles equivalent circuit model used fit electrochemical impedance spectroscopy (EIS) data.

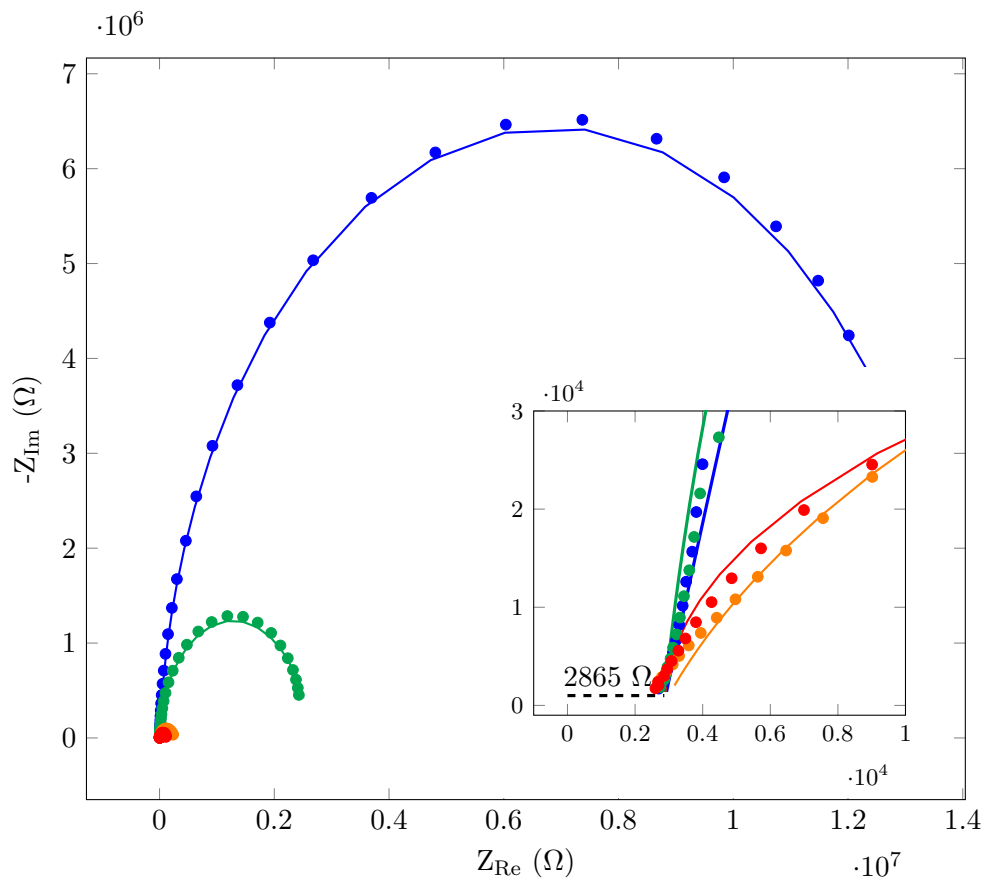


**Figure S3.** Electrochemical Impedance Spectroscopy (EIS) on Au/CXE system at ambient (0.2 MPa)  $\text{CO}_2$  pressure at various bias potentials (blue:  $-0.7$  V vs  $\text{Fc}^+/\text{Fc}$ , green:  $-1.2$  V vs  $\text{Fc}^+/\text{Fc}$ , orange:  $-2.2$  V vs  $\text{Fc}^+/\text{Fc}$ , red:  $-2.7$  V vs  $\text{Fc}^+/\text{Fc}$ ). Points are the experimental data and lines are the optimized Randles equivalent circuit. Inlay shows the ohmic resistance of the system.

**Table S1.** Optimized Randles equivalent circuit parameters for the EIS data on the Au/CXE system at ambient (0.2 MPa)  $\text{CO}_2$  pressure at various bias potentials.

Bias Voltage	$R_s$	$R_{ct}$	$Q_0$	$n$	$\sigma$
<b>-0.7 V</b>	2850 [ $\Omega$ ]	$1.4 \times 10^7$ [ $\Omega$ ]	$1.9 \times 10^{-9}$	0.96	$<1 \times 10^6$
<b>-1.2 V</b>	2840 [ $\Omega$ ]	$2.5 \times 10^6$ [ $\Omega$ ]	$1.5 \times 10^{-9}$	0.98	$<4 \times 10^5$
<b>-2.2 V</b>	2840 [ $\Omega$ ]	$2.2 \times 10^5$ [ $\Omega$ ]	$2.7 \times 10^{-9}$	0.91	$<2 \times 10^5$
<b>-2.7 V</b>	2880 [ $\Omega$ ]	$1.1 \times 10^5$ [ $\Omega$ ]	$1.2 \times 10^{-9}$	0.99	$<100$

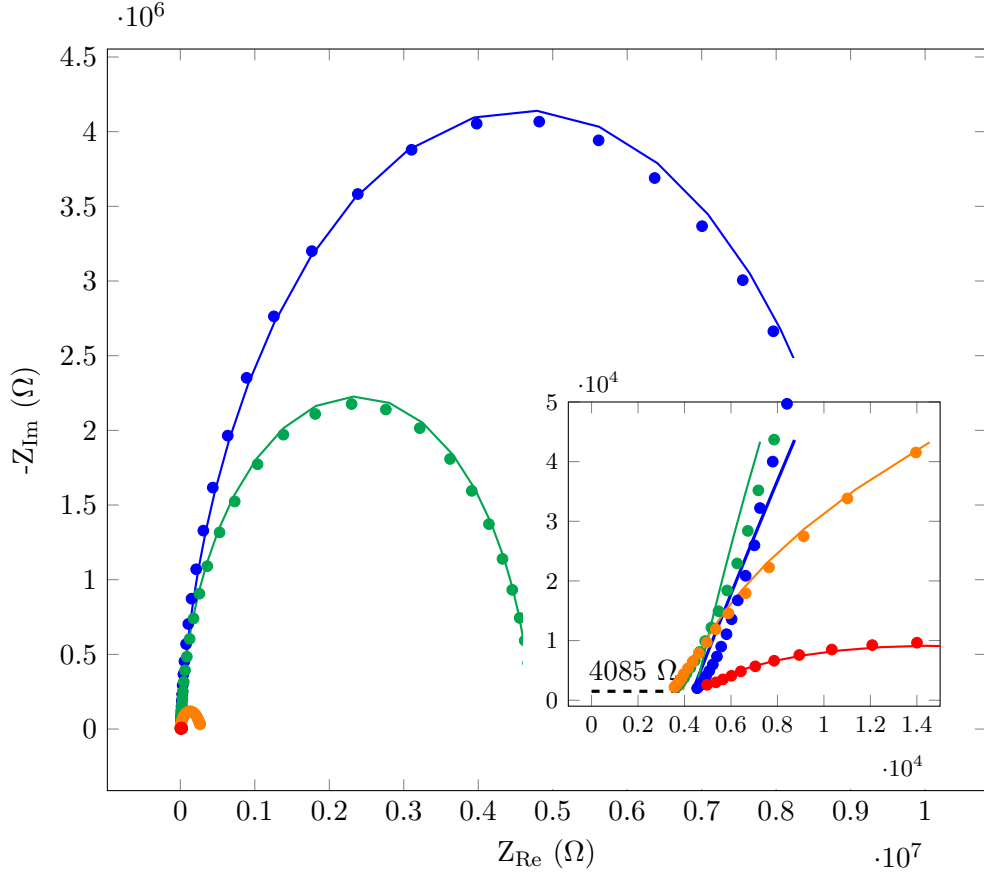


**Figure S4.** Electrochemical Impedance Spectroscopy (EIS) on Au/CXE system at 3.1 MPa CO<sub>2</sub> pressure at various bias potentials (blue: -0.7 V vs Fc<sup>+</sup>/Fc, green: -1.2 V vs Fc<sup>+</sup>/Fc, orange: -2.2 V vs Fc<sup>+</sup>/Fc, red: -2.7 V vs Fc<sup>+</sup>/Fc). Points are the experimental data and lines are the optimized Randles equivalent circuit. Inlay shows the ohmic resistance of the system.

**Table S2.** Optimized Randles equivalent circuit parameters for the EIS data on the Au/CXE system at 3.1 MPa CO<sub>2</sub> pressure at various bias potentials.

Bias Voltage	$R_s$	$R_{ct}$	$Q_0$	$n$	$\sigma$
-0.7 V	4200 [Ω]	$9.0 \times 10^6$ [Ω]	$2.1 \times 10^{-9}$	0.95	$<1 \times 10^6$
-1.2 V	4380 [Ω]	$4.7 \times 10^6$ [Ω]	$1.6 \times 10^{-9}$	0.96	$<1 \times 10^5$
-2.2 V	3800 [Ω]	$2.6 \times 10^5$ [Ω]	$1.7 \times 10^{-9}$	0.95	$<2 \times 10^4$
-2.7 V	4400 [Ω]	$2.0 \times 10^4$ [Ω]	$1.8 \times 10^{-9}$	0.93	$<100$

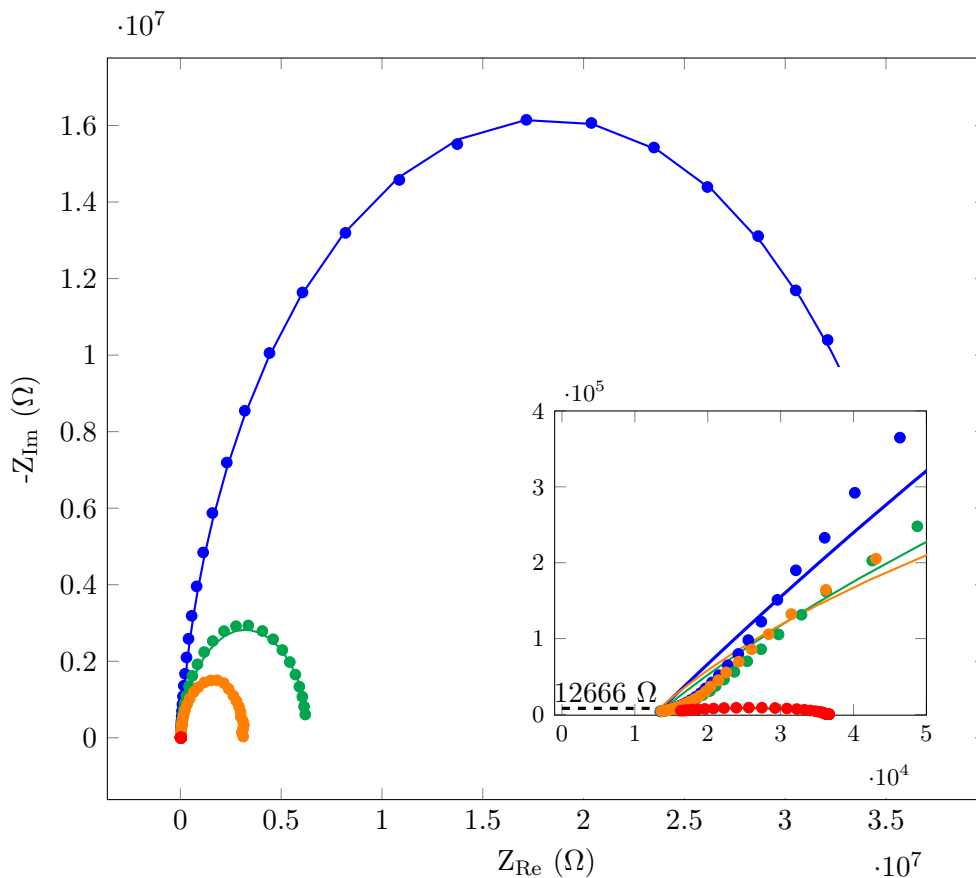


**Figure S5.** Electrochemical Impedance Spectroscopy (EIS) on Au/CXE system at 5.1 MPa CO<sub>2</sub> pressure at various bias potentials (blue: -0.7 V vs Fc<sup>+</sup>/Fc, green: -1.2 V vs Fc<sup>+</sup>/Fc, orange: -2.2 V vs Fc<sup>+</sup>/Fc, red: -2.7 V vs Fc<sup>+</sup>/Fc). Points are the experimental data and lines are the optimized Randles equivalent circuit. Inlay shows the ohmic resistance of the system.

**Table S3.** Optimized Randles equivalent circuit parameters for the EIS data on the Au/CXE system at 5.1 MPa CO<sub>2</sub> pressure at various bias potentials.

Bias Voltage	$R_s$	$R_{ct}$	$Q_0$	$n$	$\sigma$
-0.7 V	12800 [Ω]	$3.5 \times 10^7$ [Ω]	$2.2 \times 10^{-9}$	0.93	$<3 \times 10^6$
-1.2 V	13000 [Ω]	$6.5 \times 10^6$ [Ω]	$2.1 \times 10^{-9}$	0.92	$<1 \times 10^4$
-2.2 V	12500 [Ω]	$3.2 \times 10^6$ [Ω]	$2.0 \times 10^{-9}$	0.93	$<1 \times 10^4$
-2.7 V	13000 [Ω]	$2.5 \times 10^4$ [Ω]	$8.5 \times 10^{-9}$	0.76	$<1 \times 10^3$

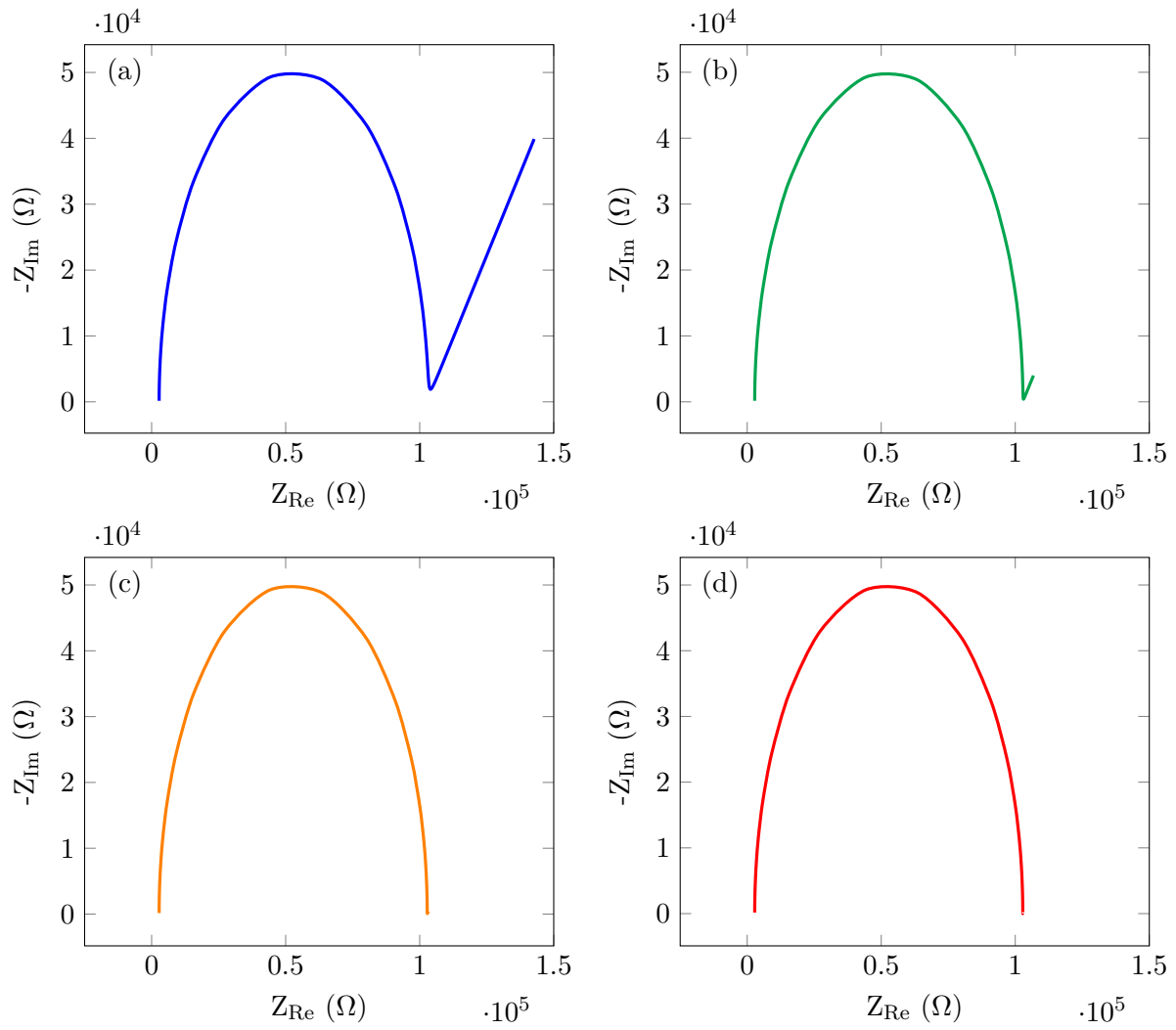


**Figure S6.** Simulated Electrochemical Impedance Spectroscopy (EIS) data of a Randles circuit showing the effect Warburg coefficient ( $\sigma$ ). For each simulation:  $R_s = 2800 \Omega$ ,  $R_{ct} = 1 \times 10^5 \Omega$ ,  $Q_0 = 1 \times 10^{-9}$ ,  $n = 1$ . (a)  $\sigma = 1 \times 10^4$ , (b)  $\sigma = 1 \times 10^3$ , (c)  $\sigma = 100$ , (d)  $\sigma = 10$ .

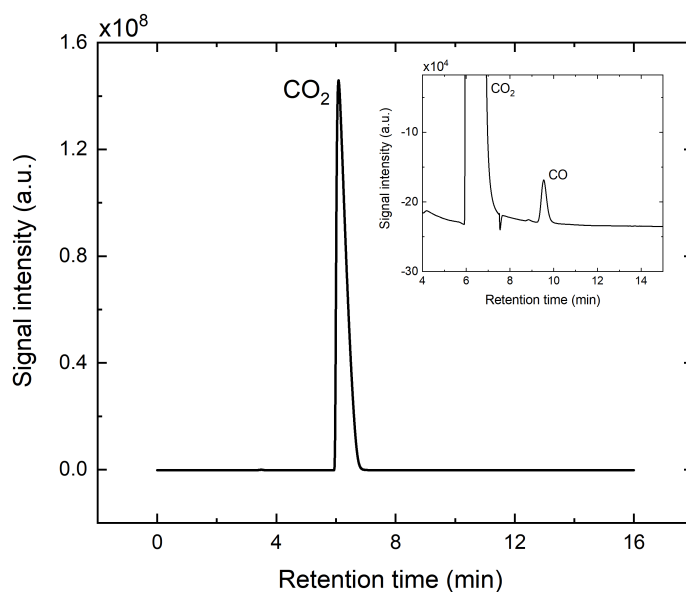


**Figure S7.** Gas-phase product detection on the Cu/CXE system at 3.1 MPa CO<sub>2</sub> pressure. Depicted is the data from the flame ionization detector channel of a calibrated gas chromatograph equipped with a methanizer. Polarization at  $-2.5$  V vs.  $\text{Fc}^+/\text{Fc}$  for 14 h. CO production rate of  $8.6 \mu\text{mol h}^{-1}$  at a Faradaic Efficiency of 35%. No other major products were detected in the gas phase.

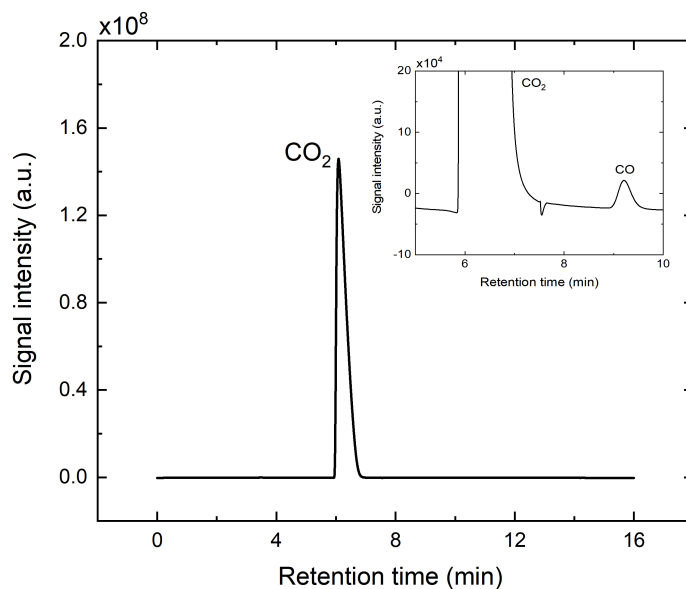


**Figure S8.** Gas-phase product detection on the Cu/CXE system at 5.1 MPa CO<sub>2</sub> pressure. Depicted is the data from the flame ionization detector channel of a calibrated gas chromatograph equipped with a methanizer. Polarization at  $-2.5$  V vs.  $\text{Fc}^+/\text{Fc}$  for 14 h. CO production rate of  $6.0 \mu\text{mol h}^{-1}$  at a Faradaic Efficiency of 28%. No other major products were detected in the gas phase.

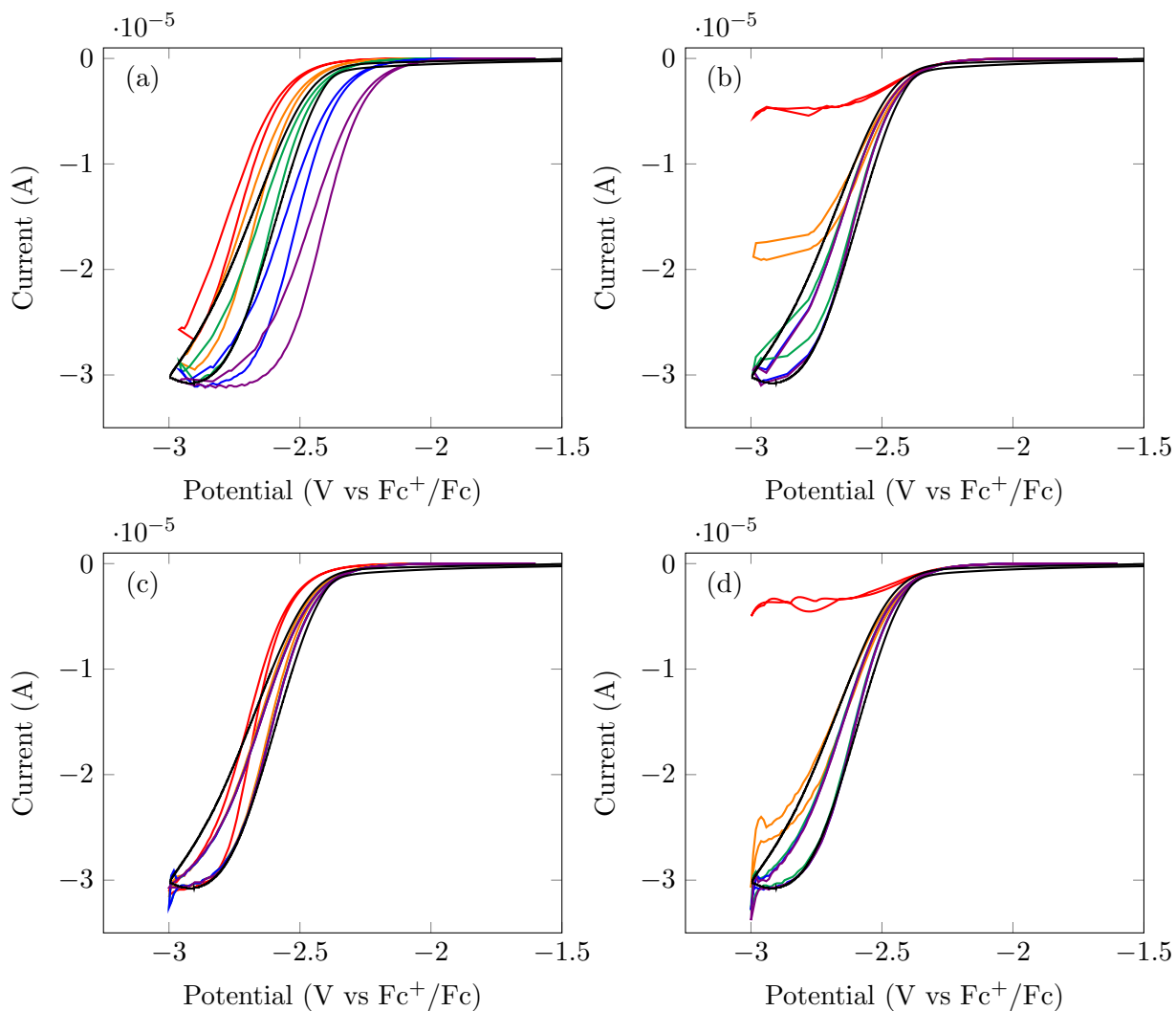


**Figure S9.** Understanding the rate determining step under atmospheric conditions (0.08 M CO<sub>2</sub> concentration). (a) Varying  $k_1^0$  (Red:  $2 \times 10^{-10} \text{ mol}^{-1} \text{ s}^{-1} \text{ m}^3$ , Orange:  $2 \times 10^{-9} \text{ mol}^{-1} \text{ s}^{-1} \text{ m}^3$ , Green:  $2 \times 10^{-8} \text{ mol}^{-1} \text{ s}^{-1} \text{ m}^3$ , Blue:  $2 \times 10^{-7} \text{ mol}^{-1} \text{ s}^{-1} \text{ m}^3$ , Violet:  $2 \times 10^{-6} \text{ mol}^{-1} \text{ s}^{-1} \text{ m}^3$ , Black: Experimental). (b) Varying  $k_2$  (Red:  $1 \times 10^{-1} \text{ mol}^{-1} \text{ s}^{-1} \text{ m}^3$ , Orange:  $1 \text{ mol}^{-1} \text{ s}^{-1} \text{ m}^3$ , Green:  $1 \times 10^1 \text{ mol}^{-1} \text{ s}^{-1} \text{ m}^3$ , Blue:  $1 \times 10^2 \text{ mol}^{-1} \text{ s}^{-1} \text{ m}^3$ , Violet:  $1 \times 10^3 \text{ mol}^{-1} \text{ s}^{-1} \text{ m}^3$ , Black: Experimental). (c) Varying  $k_3^0$  (Red:  $8 \times 10^{-7} \text{ s}^{-1}$ , Orange:  $8 \times 10^{-6} \text{ s}^{-1}$ , Green:  $8 \times 10^{-5} \text{ s}^{-1}$ , Blue:  $8 \times 10^{-4} \text{ s}^{-1}$ , Violet:  $8 \times 10^{-3} \text{ s}^{-1}$ , Black: Experimental). (d) Varying  $k_4$  (Red:  $5 \text{ s}^{-1}$ , Orange:  $5 \times 10^1 \text{ s}^{-1}$ , Green:  $5 \times 10^2 \text{ s}^{-1}$ , Blue:  $5 \times 10^3 \text{ s}^{-1}$ , Violet:  $5 \times 10^4 \text{ s}^{-1}$ , Black: Experimental).

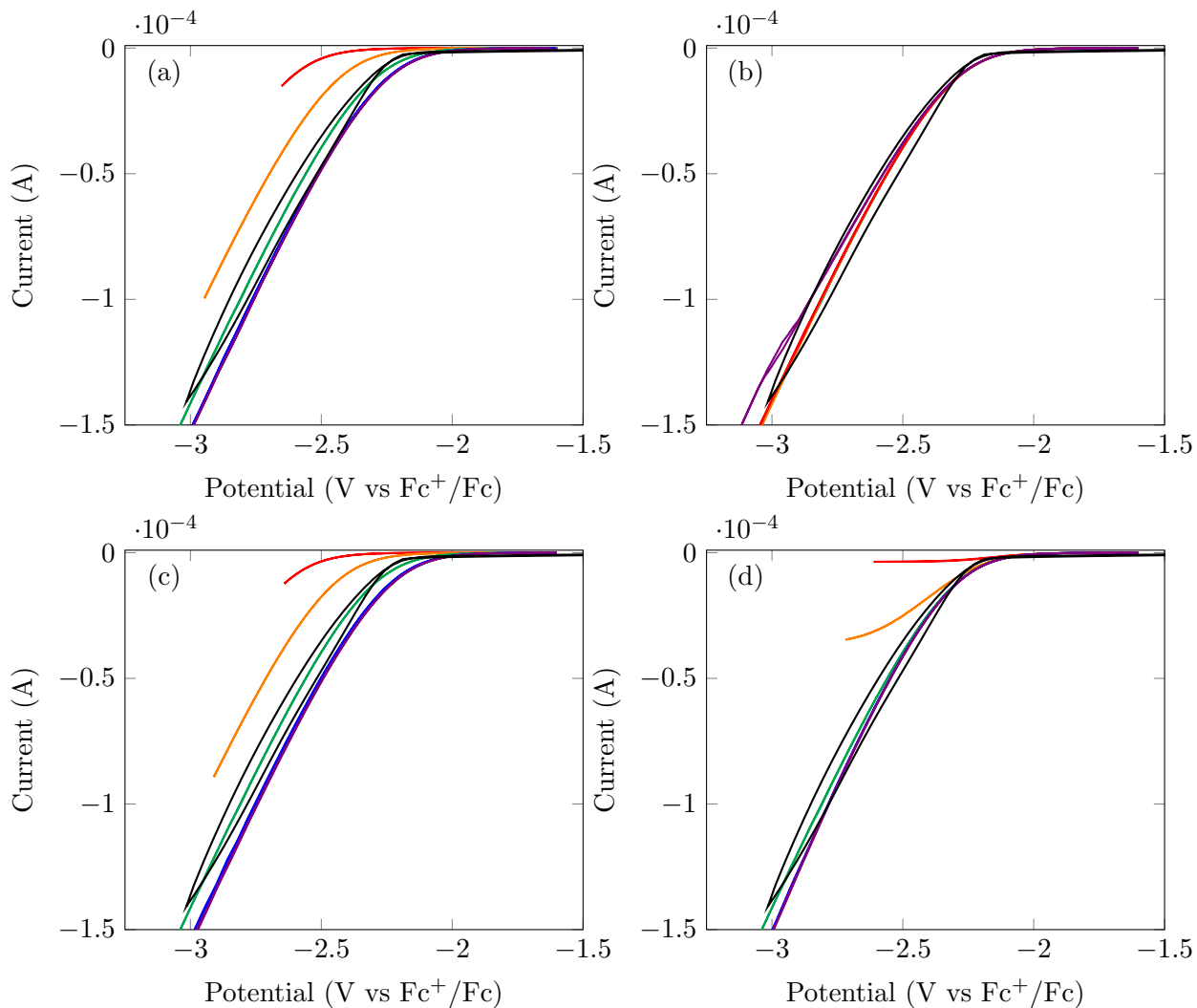


**Figure S10.** Understanding the rate determining step under 3.1 MPa CO<sub>2</sub> head-space pressure (5 M CO<sub>2</sub> concentration). (a) Varying  $k_1^0$  (Red:  $2 \times 10^{-10} \text{ mol}^{-1} \text{ s}^{-1} \text{ m}^3$ , Orange:  $2 \times 10^{-9} \text{ mol}^{-1} \text{ s}^{-1} \text{ m}^3$ , Green:  $2 \times 10^{-8} \text{ mol}^{-1} \text{ s}^{-1} \text{ m}^3$ , Blue:  $2 \times 10^{-7} \text{ mol}^{-1} \text{ s}^{-1} \text{ m}^3$ , Violet:  $2 \times 10^{-6} \text{ mol}^{-1} \text{ s}^{-1} \text{ m}^3$ , Black: Experimental). (b) Varying  $k_2$  (Red:  $1 \times 10^{-1} \text{ mol}^{-1} \text{ s}^{-1} \text{ m}^3$ , Orange:  $1 \text{ mol}^{-1} \text{ s}^{-1} \text{ m}^3$ , Green:  $1 \times 10^1 \text{ mol}^{-1} \text{ s}^{-1} \text{ m}^3$ , Blue:  $1 \times 10^2 \text{ mol}^{-1} \text{ s}^{-1} \text{ m}^3$ , Violet:  $1 \times 10^3 \text{ mol}^{-1} \text{ s}^{-1} \text{ m}^3$ , Black: Experimental). (c) Varying  $k_3^0$  (Red:  $8 \times 10^{-7} \text{ s}^{-1}$ , Orange:  $8 \times 10^{-6} \text{ s}^{-1}$ , Green:  $8 \times 10^{-5} \text{ s}^{-1}$ , Blue:  $8 \times 10^{-4} \text{ s}^{-1}$ , Violet:  $8 \times 10^{-3} \text{ s}^{-1}$ , Black: Experimental). (d) Varying  $k_4$  (Red:  $5 \text{ s}^{-1}$ , Orange:  $5 \times 10^1 \text{ s}^{-1}$ , Green:  $5 \times 10^2 \text{ s}^{-1}$ , Blue:  $5 \times 10^3 \text{ s}^{-1}$ , Violet:  $5 \times 10^4 \text{ s}^{-1}$ , Black: Experimental).

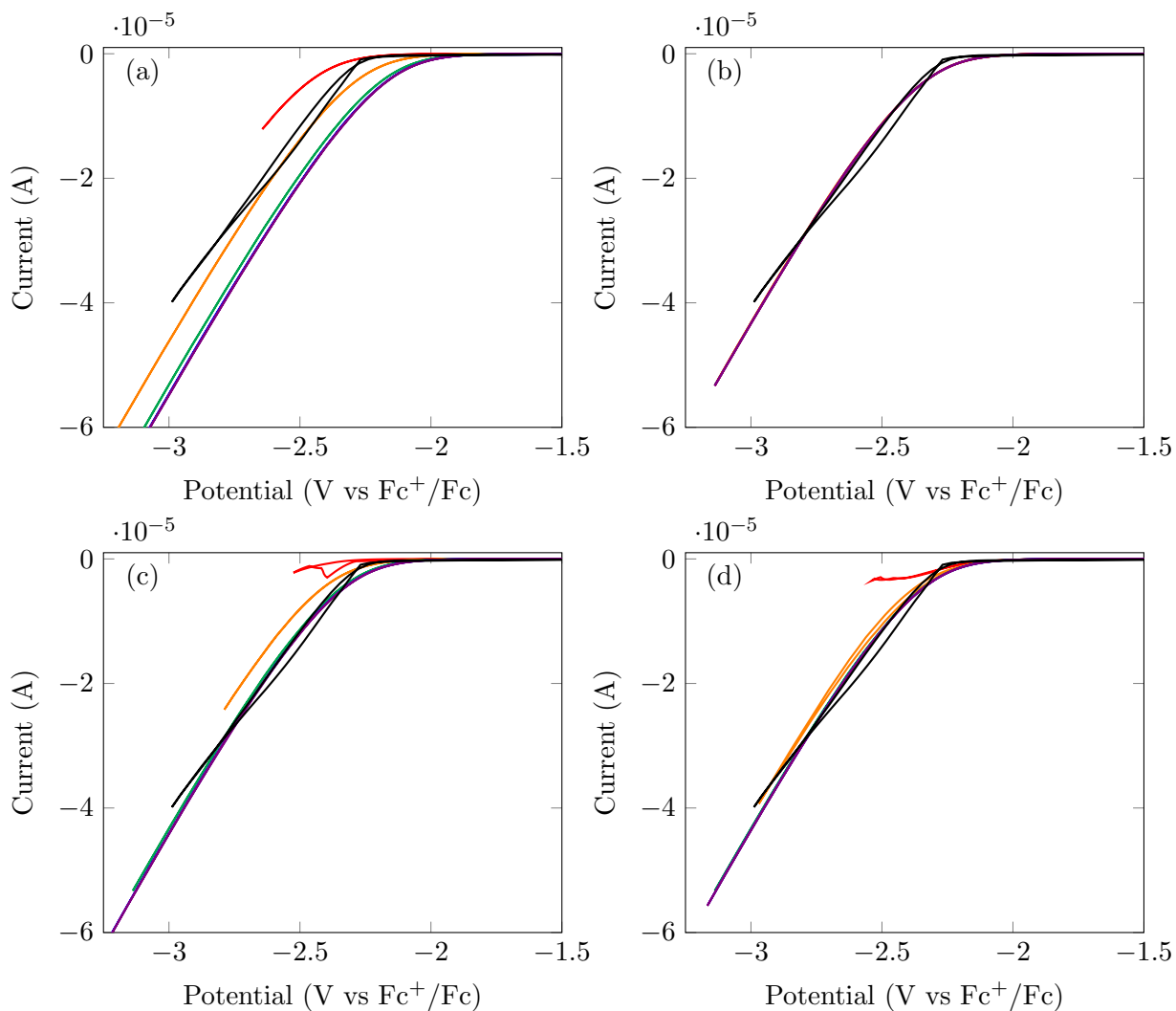


**Figure S11.** Understanding the rate determining step under 5.1 MPa CO<sub>2</sub> head-space pressure (138 M CO<sub>2</sub> concentration). (a) Varying  $k_1^0$  (Red:  $2 \times 10^{-10} \text{ mol}^{-1} \text{ s}^{-1} \text{ m}^3$ , Orange:  $2 \times 10^{-9} \text{ mol}^{-1} \text{ s}^{-1} \text{ m}^3$ , Green:  $2 \times 10^{-8} \text{ mol}^{-1} \text{ s}^{-1} \text{ m}^3$ , Blue:  $2 \times 10^{-7} \text{ mol}^{-1} \text{ s}^{-1} \text{ m}^3$ , Violet:  $2 \times 10^{-6} \text{ mol}^{-1} \text{ s}^{-1} \text{ m}^3$ , Black: Experimental). (b) Varying  $k_2$  (Red:  $1 \times 10^{-1} \text{ mol}^{-1} \text{ s}^{-1} \text{ m}^3$ , Orange:  $1 \text{ mol}^{-1} \text{ s}^{-1} \text{ m}^3$ , Green:  $1 \times 10^1 \text{ mol}^{-1} \text{ s}^{-1} \text{ m}^3$ , Blue:  $1 \times 10^2 \text{ mol}^{-1} \text{ s}^{-1} \text{ m}^3$ , Violet:  $1 \times 10^3 \text{ mol}^{-1} \text{ s}^{-1} \text{ m}^3$ , Black: Experimental). (c) Varying  $k_3^0$  (Red:  $8 \times 10^{-7} \text{ s}^{-1}$ , Orange:  $8 \times 10^{-6} \text{ s}^{-1}$ , Green:  $8 \times 10^{-5} \text{ s}^{-1}$ , Blue:  $8 \times 10^{-4} \text{ s}^{-1}$ , Violet:  $8 \times 10^{-3} \text{ s}^{-1}$ , Black: Experimental). (d) Varying  $k_4$  (Red:  $5 \text{ s}^{-1}$ , Orange:  $5 \times 10^1 \text{ s}^{-1}$ , Green:  $5 \times 10^2 \text{ s}^{-1}$ , Blue:  $5 \times 10^3 \text{ s}^{-1}$ , Violet:  $5 \times 10^4 \text{ s}^{-1}$ , Black: Experimental).

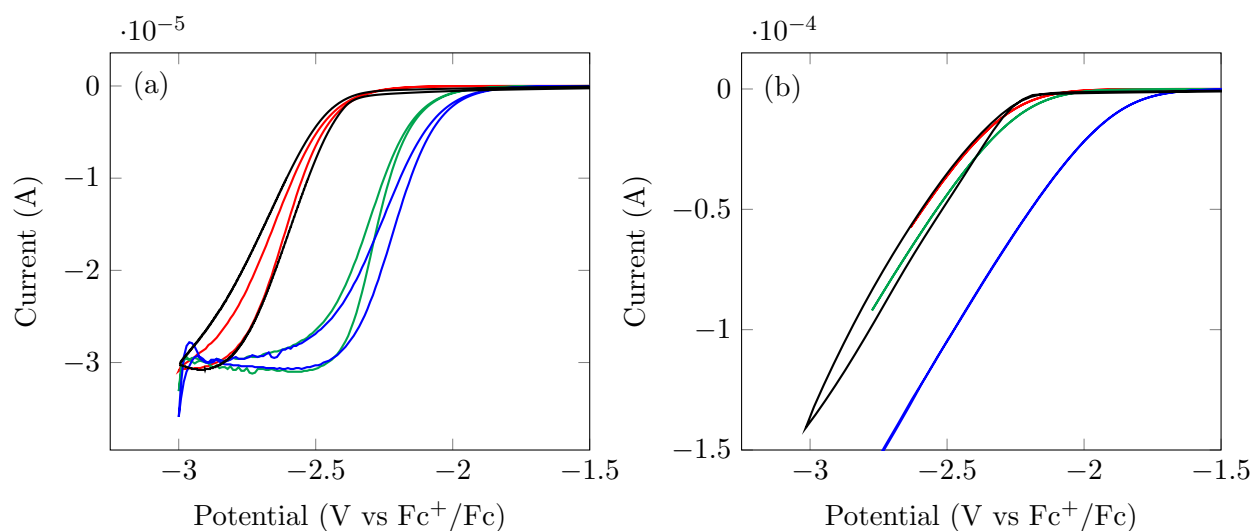


**Figure S12.** Understanding the interplay between  $k_1^0$  and  $k_3^0$  at different CO<sub>2</sub> pressures. (a) Atmospheric CO<sub>2</sub> concentration. (b) 3.1 MPa CO<sub>2</sub> concentration. (Red:  $k_1^0 = 2 \times 10^{-8} \text{ m}^3 \text{ mol s}^{-1}$  and  $k_3^0 = 8 \times 10^{-5} \text{ s}^{-1}$ , Green:  $k_1^0 = 2 \times 10^{-6} \text{ m}^3 \text{ mol s}^{-1}$  and  $k_3^0 = 8 \times 10^{-5} \text{ s}^{-1}$ , Blue:  $k_1^0 = 2 \times 10^{-6} \text{ m}^3 \text{ mol s}^{-1}$  and  $k_3^0 = 8 \times 10^{-3} \text{ s}^{-1}$ , Black: Experimental).

## Supporting References

- (1) K. Knudsen, 2019, DOI: [10.5281/zenodo.2535951](https://doi.org/10.5281/zenodo.2535951).